Characterization of High-Temperature Proton-Exchange Membranes Based on Phosphotungstic Acid Functionalized Mesoporous Silica Nanocomposites for Fuel Cells

2 **AUTHORS**, INCLUDING:

San Ping Jiang
Curtin University

345 PUBLICATIONS **11,424** CITATIONS

SEE PROFILE

Characterization of High-Temperature Proton-Exchange Membranes Based on Phosphotungstic Acid Functionalized Mesoporous Silica Nanocomposites for Fuel Cells

Jie Zeng[†,‡] and San Ping Jiang*[†]

[†]Fuels and Energy Technology Institute, Curtin University, Perth, Western Australia 6845, Australia

[‡]School of Mechanical and Aerospace Engineering, Nanyang Technological University, Singapore 639798

ABSTRACT: The synthesis and characteristics of high-temperature proton-exchange membranes based on mesoporous silica nanocomposite functionalized with phosphotungstic acid (HPW) were investigated in detail for applications in proton-exchange membrane fuel cells (PEMFCs) and direct methanol fuel cells (DMFCs). The HPW—meso-silica nanocomposites were characterized by small-angle X-ray scattering (SAXS), FTIR spectroscopy, Raman spectroscopy, TGA, N_2 absorption isotherm, water uptake, TEM, conductivity, and fuel cell performance. The spectroscopy results indicate interactions between the Keggin anions of HPW and meso-silica and the possible formation of $(\equiv SiOH_2^+)(H_2PW_{12}O_{40}^-)$ species. The results show that the proton conductivity of the HPW—meso-silica nanocomposites depends strongly on the content of HPW. The threshold for the proton conductivity of the nanocomposite is ~10 wt %. The best proton conductivity is 0.07 S cm^{-1} at 25 °C under 100% relative humidity (RH) with an activation energy of ~14 kJ mol^{-1}, obtained on HPW—meso-silica nanocomposites with 67—83% HPW. A PEMFC based on a HPW—meso-silica membrane produced a power output of 308 mW cm^{-2} at 80 °C and 80% RH in H_2/O_2, 206 mW cm^{-2} at 80 °C and 80% RH in H_2/air, and 134 mW cm^{-2} at 160 °C in methanol/air without external humidification. The high tolerance of HPW—meso-silica nanocomposites toward RH fluctuations demonstrates the unique high water retention capability of HPW—meso-silica nanocomposites. The results indicate that HPW—meso-silica forms a promising proton-exchange membrane for PEMFCs and DMFCs operating at high temperatures.
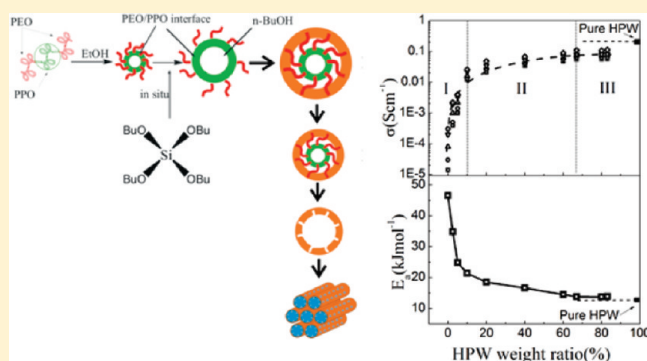
1. INTRODUCTION

Proton-exchange membrane fuel cells (PEMFCs) have been considered as an attractive energy source for both portable and automobile applications because of their high energy conversion efficiency, high power density, quiet operation, and low greenhouse gas emissions.[1,2] The efficiency and performance of PEMFCs can be further enhanced by increasing the operating temperature of the fuel cells to 120—200 °C because of the improved reaction kinetics and significantly reduced catalyst poisoning by CO.[3—5] Water and heat management of fuel cell systems becomes easier at high temperatures. Direct methanol fuel cells (DMFCs) also benefit significantly from increased operation temperatures.[6,7] However, the proton conductivity of state-of-the-art perfluorosulfonic acid (PFSA) membranes such as Nafion depends strongly on the water content of the membrane and decreases significantly with increasing temperature or decreasing relative humidity because of the loss of water from the membrane under conditions of high temperature or low humidities.[8—13] Thus, the grand challenge is to develop proton-exchange membranes (PEMs) with high conductivity and stability at high temperatures (>100 °C) and low humidity.

It is known that heteropolyacids (HPAs) are superionic conductors in their fully hydrated states.[14,15] HPAs are solid crystalline materials with polyoxometalate inorganic cage structures that can adopt the Keggin form with general formula $H_3MX_{12}O_{40}$, where typically M = P or Si and X = W or Mo. The highest stability and strongest acidity is observed for phosphotungstic acid ($H_3PW_{12}O_{40}$, abbreviated as HPW or PWA). Because of their high acidity, stability, and high proton conductivity, HPAs have been used as additives to promote the electrocatalytic activities of electrocatalysts for methanol oxidation,[16—19] ethanol oxidation,[20,21] and oxygen reduction.[22—25] However, the application of HPAs as proton-exchange membranes in fuel cells is limited because of the sensitivity of their conductivity to the relative humidity of the surrounding environment in addition to their solubility in water. The risk of the leakage of HPAs during cell operation is thus high. Various attempts have been made to immobilize HPAs in silica gel,[26—28]

ammonium salt,[29] and $P_2O_5-SiO_2$ glasses;[30,31] to form HPW composites with room-temperature ionic liquids;[32] and to form hybrid organic/inorganic membranes.[33−37] Lakshminarayana and Nogami mixed HPW and phosphomolybdic acid (HPMo) with 3-glycidoxypropyltrimethoxysilane (GPTMS), 3-aminopropyltriethoxysilane (APTES), phosphoric acid, and tetraethoxysilane (TEOS) by a sol−gel process and reported a proton conductivity of 3×10^{-2} S cm^{-1} with a composition of 50 TEOS/25 GPTMS/20 H_3PO_4/5 APTES/3 HPMo/6 HPW at 120 °C under 90% relative humidity (RH).[38] Sweikart et al. mechanically mixed HPW and commercially available high-temperature epoxy (Duralco 4538N) and reported a conductivity of 6×10^{-5} S cm^{-1} at 165 °C without humidification for a HPW-doped sulfonated epoxy.[39] The conductivity of mixed HPW/epoxy hybrid membranes is too low for practical fuel cell applications. Tan et al. synthesized composite membranes containing sulfonated poly(arylene ether sulfone) (SPSU), benzimidazole derivatives (BIzD), and HPW.[40] Adding BIzD helps to retain HPW particles, and good conductivity was reported for the SPSU−BIzD−HPW hybrid membranes (0.084−0.159 S cm^{-1} at 110 °C under fully hydrated conditions). High proton conductivity and excellent cell performance of 510 mW cm^{-2} at 120 °C were also reported on Nafion−HPW/meso-silica hybrid membranes.[12] However, high swelling ratios associated with polymeric materials are detrimental to the structural stability of the membranes.

Surfactant template mesoporous materials such as mesoporous silica have attracted a great deal of attention because of the tunable mesoporous structure. High specific surface area, nanosized channels or frameworks with an ordered and interconnected internal structure, and high structural stability allow their potential applications as proton-exchange membranes operating at elevated temperatures.[30,41−49] Capillary condensation would occur favorably in meso- or nanosized hydrophilic channels or pores, and the saturation vapor pressure decreases with decreasing capillary diameter, resulting in water condensation at reduced humidity.[50] Rao et al. studied the HPW in alumina-grafted silica gel and mesoporous SBA-15 silica by impregnation, and the results show that the high surface area and high surface concentration of silanols in SBA-15 are beneficial for the immobilization of HPW catalysts.[27] We showed recently that HPW can be incorporated into the mesoporous silica matrix by impregnation or by a one-step synthesis process, forming immobilized HPW nanoparticles/clusters in the mesoporous silica matrix.[51,52] The proton conductivity of HPW-functionalized mesoporous silica, MCM-41, reached 0.018 and 0.045 S cm^{-1} at 25 and 150 °C, respectively. Thus, the combination of the mesoporous silica matrix and proton-conducting HPW would offer a promising potential candidate as high-temperature PEMs for fuel cells. Here, we studied in detail the relationships between the HPW content, the proton conductivity and stability, and the cell performance of HPW-functionalized mesoporous silica with cubic bicontinuous structure ($Ia\bar{3}d$). The results demonstrate that the proton conductivity of HPW−meso-silica nanocomposites depends strongly on the HPW content and that the threshold for the proton conductivity is ~10 wt %. The HPW−meso-silica membranes exhibited a proton conductivity as high as 0.07 S cm^{-1} at 25 °C under 100% RH. The cells employing a HPW−meso-SiO_2 electrolyte membrane produced an impressive power output in both hydrogen and methanol fuels. The results indicate that mesoporous HPW-functionalized silica nanocomposite is a promising PEM material for PEMFCs operated under high-temperature and low-humidity conditions.
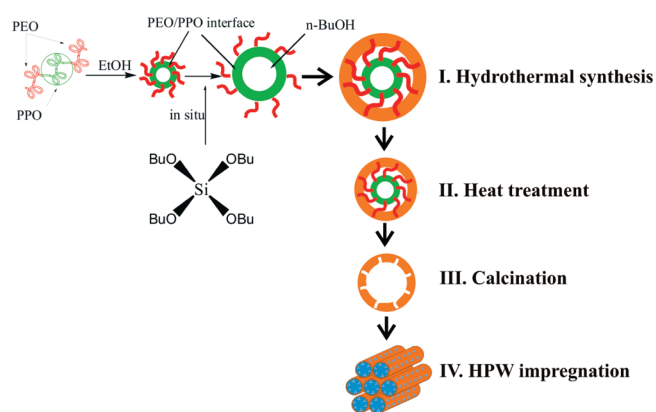

Figure 1. Procedure for the synthesis of HPW-functionalized meso-silica by the impregnation method.

2. EXPERIMENTAL SECTION

2.1. Membrane and Cell Preparation. Ordered bicontinuous cubic $Ia\bar{3}d$ mesoporous silica was prepared by using triblock copolymer P123 ($EO_{20}PO_{70}EO_{20}$, Sigma-Aldrich) as a template under acidic conditions according to the synthesis method reported by Zhao and co-workers.[53,54] Anionic surfactant sodium dodecylbenzene sulfonate (SDBS, Sigma-Aldrich) was used as an additive to induce self-assembly. SDBS (6 mM, 2.3 g) was first dissolved in a solution containing 20 g of P123, 32 g of HCl (67%), and 720 g of deionized water (18.2 MΩ) and stirred until a homogeneous solution was formed. Then, tetraethyl orthosilicate (TEOS, 43 g, Sigma-Aldrich) was added to the solution, the mixture was further stirred at 45 °C for 24 h, and then transferred into a hydrothermal reactor for hydrothermal treatment at 60 °C for another 24 h. The product was filtered and thoroughly washed with water and then air-dried overnight. The as-synthesized powder was calcined at 650 °C in air for 6 h to remove the triblock copolymer template. The calcination process started from room temperature with a ramping rate of 1 °C min^{-1}, and N_2 was used as a protective atmosphere at temperatures below 200 °C. The meso-silica was functionalized with HPW by impregnation treatment of the mesoporous silica in a HPW solution under vacuum.[51] The powder was dried at 80 °C overnight and collected. The HPW loading in the meso-silica was controlled between 2.5 and 83 wt %. Figure 1 shows the procedures for the synthesis of mesoporous silica and HPW-functionalized meso-silica by the impregnation method. HPW-functionalized meso-silica or HPW−meso-silica electrolyte disk samples for the conductivity and cell performance measurements were prepared by hot-pressing at 180 °C for 2 h. The disk samples had a diameter of 4.0 cm and a thickness of ~500 μm.

2.2. Characterization. Small-angle X-ray scattering (SAXS) spectra were obtained on a SAXSess high-flux small-angle X-ray scattering instrument (AntoPaar GmbH) equipped with a two-dimensional wire detector and a Cu ($\lambda = 0.1542$ nm) rotating anode operated at 80 kV and 40 mA. Nitrogen adsorption/desorption isotherms were measured using a Micromeritics ASAP Tristar II 3020 system. The samples were degassed at 300 °C overnight under nitrogen flow. Specific surface area was calculated using the Brunauer−Emmett−Teller (BET) method. The total pore volumes were estimated from the adsorbed amount at the relative pressure of $P/P_0 = 0.95$, and the pore size distributions were obtained from the adsorption branch of the

isotherms by using nonlinear density function theory (NLDFT) method. Ttransmission electron microscopy (TEM) micrographs were obtained using a JSM-2100F JEOL electron microscope equipped with an energy-dispersive X-ray (EDX) detector (Noran Instruments) and operated at 200 kV with a cold-field emission source. Fourier transform infrared (FTIR) absorption spectra of the pure HPW and HPW—meso-silica composite membranes were recorded with a JASCO FTIR-Q250 spectrometer (spectral range of 4000—200 cm^{-1}, 50 scans, resolution of 2 cm^{-1}). The samples were diluted in KBr (10% sample and 90% KBr) and were pressed into thin wafers for study. Thermogravimetric analysis (TGA) was carried out on a thermogravimetry/differential thermal analysis (TG/DTA) Q500 instrument from 30 to 500 °C at a heating rate of 10 °C min^{-1} under a nitrogen flow of 40 mL min^{-1}.

The water uptake of the membranes is defined as the mass ratio of absorbed water to the dry membrane. A water uptake test was carried out according to the following procedures: Hydrated samples were first dried at 40 °C under a N_2 flow overnight to remove the surface water; then, the sample was weighed, and the weight was recorded as W_{wet}. The samples were heat-treated at 200 °C under air for 24 h; after that, the samples were weighed again, and the weight was recorded as W_{dry}. The water uptake was calculated as[40]

$$\text{water uptake} = \frac{(W_{wet} - W_{dry})}{W_{dry}} \times 100\% \qquad (1)$$

The proton conductivity measurements of as-synthesized meso-silica and HPW—meso-silica nanocomposites with different HPW contents were obtained by a four-probe method, using electrochemical impedance spectroscopy (PGSTAT30/FRA, Autolab, Utrecht, The Netherlands) over the frequency range from 1 Hz to 1 MHz in the temperature range from 20 to 90 °C. The relative humidity (RH) of the proton conductivity measurements was controlled by a PEMFC test station (FCATS-G050, Greenlight, Canada).

2.3. Cell Preparation and Characterization. For the cell performance measurement, 80 wt % HPW—meso-silica nanocomposite was used as the electrolyte, and carbon paper (Toray TGPH-060) was used as the gas diffusion layer (GDL) for both anode and cathode. Single-cell hardware with a 4 cm^2 active area and graphite flow field plates were used for PEMFC and DMFC performance characterization. For the PEMFC test, the hydrogen and air (or oxygen) flow rates were 20 and 50 mL min^{-1} (10 mL min^{-1} for O_2), respectively. Pt/C (20 wt % Pt/C, E-TEC) was used as the catalyst for anode and cathode, and the Pt loading was 0.4 mg cm^{-2}. The relative humidity of the feed gas was controlled by the Greenlight PEMFC station. A cell with Nafion 115 (DuPont) membrane was also contructed and tested in H_2/O_2 at 80 °C under identical conditions.

The methanol crossover through the HPW—meso-silica nanocomposite membranes was measured using a limit current method. A HPW—meso-silica membrane was sandwiched between an anode and a cathode layer with an active electrode area of 4 cm^2; 20 wt % PtRu/C catalyst was used for the anode, and 20 wt % Pt/C catalyst was used for the cathode. The loading of Pt was about 0.4 mg cm^{-1}. Methanol solution (2 M) was fed to the anode at a flow rate of 0.5 mL min^{-1}, and dry nitrogen gas was fed to the cathode side at 50 mL min^{-1} under ambient pressure. The potential was scanned from 0.1 to 1.0 V at a scan rate of 5 mV s^{-1}, and the methanol penetrated through the membrane was
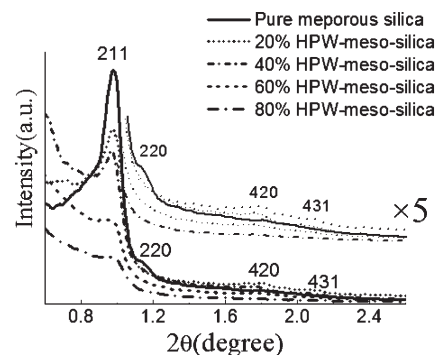

Figure 2. Small-angle X-ray scattering (SAXS) patterns of $Ia\bar{3}d$ mesoporous silica and HPW—meso-silica composites with different HPW contents.

oxidized on the cathode side. The cell temperature was stabilized for 1 h before the test. For the DMFC test, the air flow rate was 50 mL min^{-1} without humidification, and no back pressure was applied on the cathode side. The flow rate of methanol solution (2.0 M) was 0.5 mL min^{-1}. The cathode Pt loading was 2 mg cm^{-2} 50 wt % Pt/C, and the anode Pt loading was 4 mg cm^{-2} 50 wt % PtRu/C; the effective membrane area was 4 cm^2. The cell performance measurements were carried out in the temperature range of 80—160 °C. The stability of the methanol/air fuel cell was tested at 150 °C under a constant cell potential of 0.5 V for 51.5 h. The thickness of the HPW—meso-silica nanocomposite membrane was 0.5 mm.
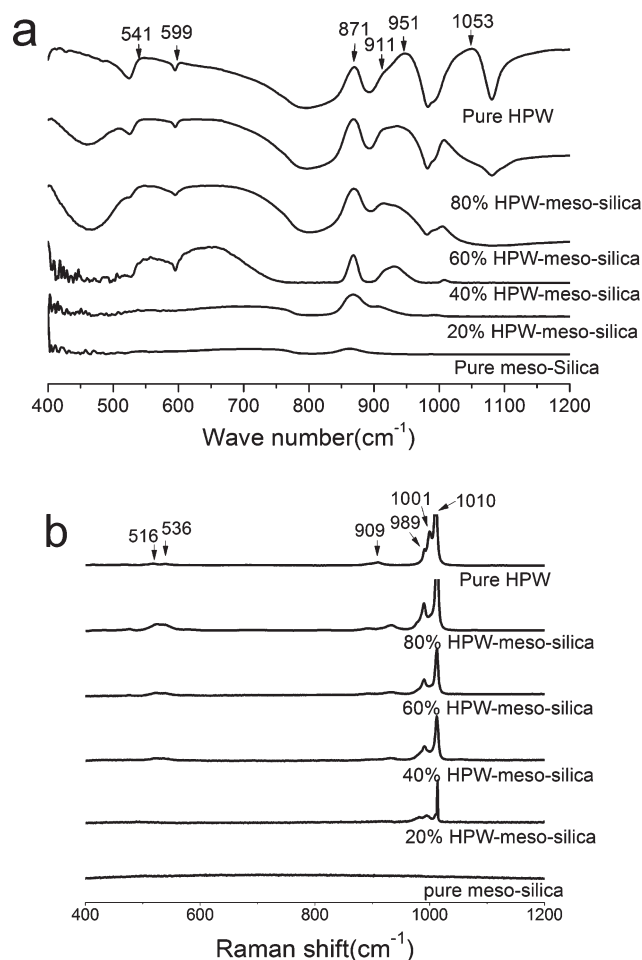
3. RESULTS AND DISCUSSION

3.1. SAXS, FTIR Spectroscopy, Raman Spectroscopy, N_2 Absorption Isotherms, and TEM. Figure 2 shows the SAXS patterns of pure mesoporous silica and HPW—meso-silica composite materials. All samples indicate well-resolved scattering peaks and characteristic SAXS patterns of mesoporous silica. For pure mesoporous silica, the SAXS curve (solid line) shows four well-resolved scattering peaks, which can be assigned to the 211, 220, 420, and 431 scattering peaks of the $Ia\bar{3}d$ structure, suggesting the successful formation of the $Ia\bar{3}d$ mesoporous silica structure.[53,55] After HPW impregnation, the relative intensities of the 211, 220, 420, and 431 scattering peaks of the $Ia\bar{3}d$ structure decrease with increasing HPW content. However, the position of the scattering peaks for HPW—meso-silica composites remains more or less the same as that of the corresponding meso-silica hosts, which implies that the symmetrical and dimensional properties of the meso-silica host are well reserved after HPW impregnation. One possible explanation for the significant decrease in the relative intensity of the scattering peak is that the impregnation of HPW molecules inside the silica mesopores reduces the contrast between the walls and pores of meso-silica, leading to a drop in the scattering intensity of SAXS. The interaction between the siliceous host and impregnated HPW molecules could be detrimental to the structural regularity of the mesoporous silica. Table 1 lists the corresponding structural parameters of HPW—meso-silica nanocomposites with different HPW contents.

The FTIR spectra of pure HPW, meso-silica, and HPW—meso-silica nanocomposites are presented in Figure 3a. HPW in the dehydrated state or in polar solvents produces stable Keggin-type anions such as $PW_{12}O_{40}{}^{3-}$, which is neutralized by three protons

11856

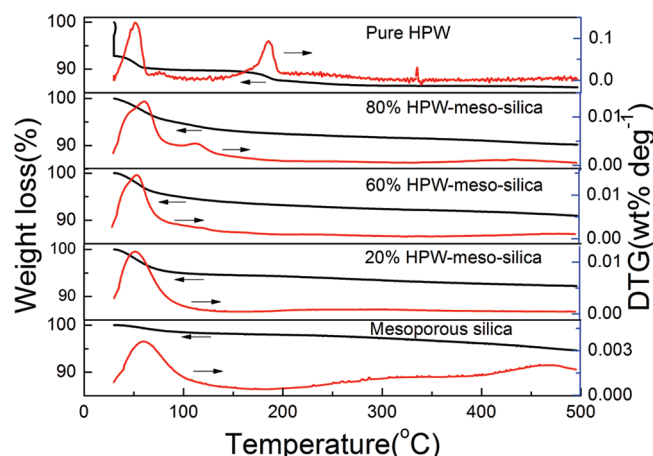dx.doi.org/10.1021/jp201250r |J. Phys. Chem. C 2011, 115, 11854–11863

Table 1. Parameters of Meso-Silica and HPW−Meso-Silica Nanocomposites with Different HPW Contents

sample	unit cell α^a (nm)	S_{BET} (m^2 g^{-1})	pore volume (cm^3 g^{-1})	pore size (nm)	wall thickness^b (nm)
meso-silica	20.5	935	1.084	5.0	5.2 ± 0.2
20% HPW−meso-silica	20.5	822	0.928	4.9	5.2 ± 0.3
40% HPW−meso-silica	20.5	679	0.643	4.2	5.6 ± 0.3
60% HPW−meso-silica	20.6	434	0.282	3.9	6.0 ± 0.3
80% HPW−meso-silica	20.8	252	0.153	3.7	6.3 ± 0.4

^{a} For cubic $Ia\bar{3}d$ pore symmetry, the unit cell parameter was obtained as $\alpha_0 = d_{211}\sqrt{6}$. ^{b} Estimated from TEM micrographs.

Figure 4. TGA spectra of HPW, meso-silica, and HPW−meso-silica nnaocomposites with different HPW contents.

Figure 3. (a) FTIR spectra and (b) Raman scattering spectra of HPW, meso-silica, and HPW−meso-silica nanocomposites measured at room temperature.

in water. This structure is formed by a central atom of phosphorus tetrahedrally linked to oxygen atoms surrounded by seven other oxygen atoms linked to a tungsten atom.[56] When hydrated water molecules are present in HPW, the terminal oxygen atoms of the Keggin anions are associated with $H_5O_2^+$, generating a secondary structure with characteristic peaks in the FTIR spectrum.[57] For pure HPW, characteristic bands are observed at 1053 cm^{-1} for P−O$_a$, 951 cm^{-1} for W=O$_d$, 911 cm^{-1} for W−O$_b$−W, and 871 cm^{-1} for W−O$_c$−W, which are close to the values reported in the literature.[58] The appearance of the characteristic peaks in the spectra of HPW−meso-silica nanocomposites indicates that the Keggin-type anions, $P_4W_{12}O_{40}^{3-}$, remain in the nanocomposite structure; in addition, the peaks in the range of 800−1000 cm^{-1} are partially

overlapped by the $\delta(Si-O-Si)$ stretching, as well as the OH bending of the O_3Si-H group from the mesoporous silica framework. In the spectra of the samples with various HPW contents, one can observe a broadening and progressive shift of the band at 951 cm^{-1} as the HPW contents increase from 20% to 80%; the frequency shift reveals a possible interaction between the Keggin anions of HPW and the silanols on the silica surface. Dias et al. studied HPW-impregnated mesoporous silica by ^{31}P solid-state nuclear magnetic resonance (NMR) spectroscopy and observed the chemical shift of the ^{31}P NMR peak from 15.5 ppm for pure HPW to 15.0 ppm for the HPW-impregnated meso-silica.[59] The chemical shift in the ^{31}P NMR spectra was attributed to the formation of $(\equiv SiOH_2^+)(H_2PW_{12}O_{40}^-)$ species.[60] The increased intensity of the new peak at ∼1011 cm^{-1} with the increase in HPW content can be associated with the formation of $(\equiv SiOH_2^+)(H_2PW_{12}O_{40}^-)$ species.

The Raman scattering spectra of pure HPW, meso-silica, and HPW/meso-silica nanocomposite are shown in Figure 3b. The spectrum of pure HPW is characterized by bands at 1001 and 989 cm^{-1}, which are assigned to antisymmetric and symmetric stretching modes, respectively, of octahedral W−O.[58] Both are the signatures of the Keggin structure and are in agreement with the FTIR results. A peak typical of the Keggin structure (i.e., the asymmetric stretching vibration of the central PO$_4$ tetrahedran) at 1010 cm^{-1} was partially overlaid by the Si−O framework vibrations. The appearance of these characteristic peaks in the spectrum of HPW−meso-silica composite indicates that the structure of the heteropolyanions $P_4W_{12}O_{40}^{3-}$ remains intact in the composite material.

Figure 4 shows the TG thermograms of pure HPW, mesoporous silica, and HPW−meso-silica measured in the temperature range of 30−500 °C. The TGA curve of pure HPW exhibits two
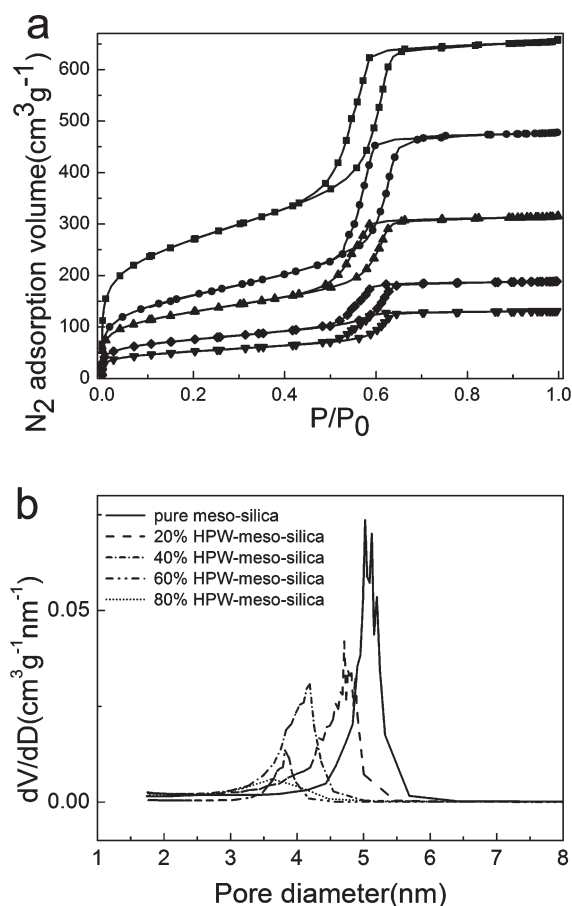
Figure 5. (a) N$_2$ absorption isotherms and (b) pore size distribution of (■) meso-silica and (●) 20%, (▲) 40%, (◆) 60%, and (▼) 80% HPW−meso-silica nanocomposites.

Figure 6. TEM images of (a) pure meso-silica and (b) 20% and (c) 80% HPW−meso-silica. The left images were viewed from the [110] direction, whereas the right images were viewed from the [111] direction.

weight loss steps at temperatures around 50 and 186 °C, which is in agreement with the values reported in the literature.[33,39] The first weight loss between room temperature and 70 °C can be attributed to the loss of physically absorbed water, and the second one between 160 and 200 °C can be assigned to the release of more structural water from HPW hydrate. The weight loss of HPW at 200 °C was 14.6%. The retention of water molecules by the Keggin-type HPW structure at high temperatures indicates the possibility of proton conductivity at high temperatures. On the other hand, the $Ia\bar{3}d$ meso-silica shows only one weight loss steps at ∼65 °C, and the weight loss is ∼1.0% at 200 °C, much lower than 14.6% for pure HPW. The thermal behavior of HPW−meso-silica nanocomposite is significantly different from that of pure HPW. For example, in the case of 80% HPW−meso-silica nanocomposite, the dehydration peak of structural water of pure HPW at 186 °C disappears, and the weight loss at 200 °C is 7.2% for 80 wt % HPW−meso-silica, which is lower than the 14.6% observed for pure HPW, but significantly higher than the 1% observed for pure meso-silica. The disappearance of the dehydration peak at high temperatures suggests that the homogeneous distribution of HPW in the mesoporous silica host changes the behavior of water molecules in the HPW Keggin structure and enhances the stability of water in the HPW−meso-silica system.

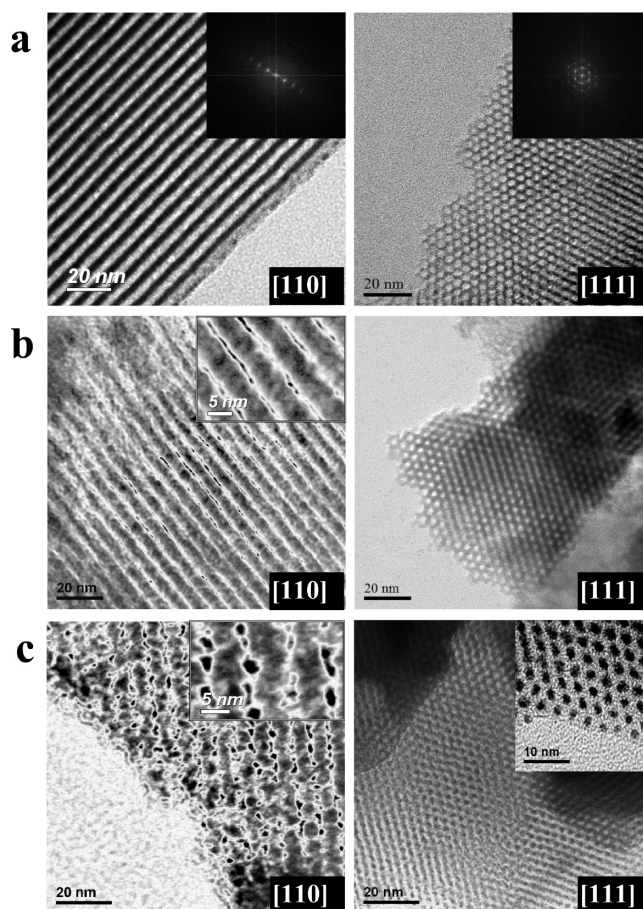The pore size and pore volume of meso-silica and HPW−meso-silica nanocomposites with different HPW contents were evaluated by nitrogen adsorption−desorption isotherm measurements, and the results are shown in Figure 5. The N$_2$ sorption isotherms (Figure 5a) show typical type-IV characteristics associated with a distinct and sharp step at a relative pressure of ∼0.58. The sharp step in the adsorption isotherm indicates capillary condensation because the pore size distribution is very uniform.[61] The analysis of the adsorption isotherms with the BET method gives surface areas in the range of 935 m^2 g^{-1} for pure meso-silica, which is larger than 822 m^2 g^{-1} reported for mesoporous SBA-15 silica.[27] On the other hand, the surface area and pore volume of the HPW−meso-silica composite are reduced significantly with the impregnation of HPW into meso-silica matrix. As the impregnated HPW loading increased from 0 to 80 wt %, the surface of the meso-silica host decreased from 935 to 252 m^2 g^{-1}, whereas the pore volume decreased from 1.084 to 0.153 cm^3 g^{-1}, indicating the filling of the mesoporous channels of the silica by the impregnated HPW particles.

As compared with that of meso-silica hosts, it appears that the N$_2$ sorption isotherms of HPW−meso-silica nanocomposite exhibits a much wider hysteresis loop, suggesting a smaller pore entrance for the HPW−meso-silica nanocomposite. The reason could be that the impregnated HPW partially blocks the pore entrance of nanochannel structure of meso-silica.[62] Figure 5b shows the pore size distribution obtained by nonlinear density function theory (NLDFT), which also indicates a significant
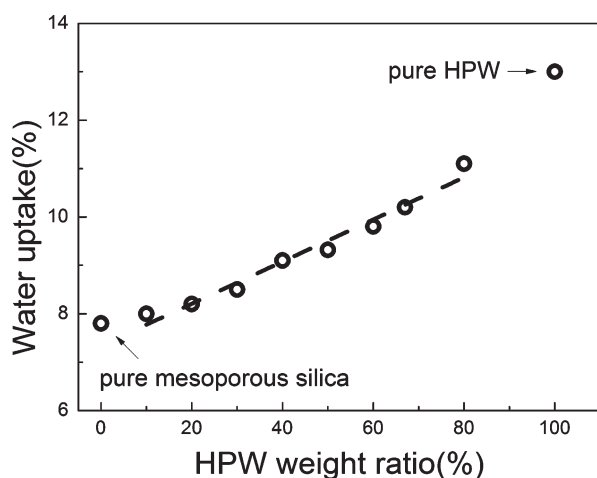
Figure 7. Water uptake of HPW−meso-silica nanocomposites as a function of HPW content.

drop in the pore diameter from 5.0 to 3.7 nm as the HPW loading increased from 0 to 80 wt %, implying that most of the void space existing in the original host was occupied by the impregnated HPW particles. The pore sizes, pore volumes, and BET surface areas of HPW−meso-silica nanocomposites with different HPW contents are given in Table 1.

The microstructure of mesoporous silica and HPW−meso-silica nanocomposite were studied by TEM and the results are shown in Figure 6. The mesoporous silica host was characterized by highly ordered nanochannels as shown in Figure 6a. The TEM images (from left to right) of Figure 6a were taken from the [110] and [111] direction, which can be confirmed by the corresponding FFT images (see the inset in Figure 6a). The TEM image taken along the pore axis (i.e., [111] direction) indicates that the channel diameter of mesoporous silica is ∼5.2 nm, which is consistent with the N$_2$ absorption isotherm result of 5.0 nm.

In the case of HPW−meso-silica nanocomposites, the TEM images provide a direct observation of the morphology and distribution of the impregnated HPW nanoparticles in the mesoporous silica matrix, indicated by the ordered but not continuous black dots sandwiched between continuous channels (gray in color, see Figure 6b,c). The thick line structure in gray color is siliceous pore walls, and the color difference between the black dots and gray thick line structures is due to the phase contrast between HPW and silica (tungsten atoms of HPW are much heavier than silicon atoms of silica). The phase contrast becomes pronounced as the HPW content in the nanocomposite increased to 80% (see the inset, Figure 6c). Such phase contrast was also observed in the cesium-substituted HPA−meso-silica system.[63] As the HPW content in meso-silica increased to 80 wt %, the density of HPW particles (i.e, the black dots, see Figure 6c) increased, indicating that the distribution of HPW particles in 80% HPW−meso-silica is much more uniform than that in 20% HPW−meso-silica (Figure 6b). The higher intensity of HPW particles inside the meso-silica means a shorter pathway of proton transportation, which would lead to the high proton conductivity and low activation energy barriers for proton conductance in the meso-silica matrix. The average distances between the HPW particles in the HPW−meso-silica nanocomposites vary between 0 to 5 nm, and the shape and diameter of the interconnected channels of HPW−meso-silica nanocompo-

sites are not as regular as those of the pristine meso-silica host (Figure 6c inset), because of the impregnation and insertion of HPW particles.

3.2. Water Uptake and Conductivity of the HPW−Meso-Silica Nanocomposites. Figure 7 shows the water uptake results for HPW−meso-silica nanocomposite as a function of HPW content. The water uptake of meso-silica is ∼8%, and it increases almost linearly with the impregnated HPW content. As the HPW content increased to 80 wt %, the water uptake of the HPW−meso-silica nanocomposite is ∼11%, which was slightly low than ∼13% for pure HPW under the conditions studied. No change in the sample dimensions during the water uptake tests was observed, and swelling of the HPW−meso-silica nanocomposite was negligible. The high water content in the HPW−meso-silica as compared to that of meso-silica indicates the significantly enhanced water retention ability of the impregnated HPW in the mesoporous silica matrix. In the case of Nafion-based membranes, the water uptake can be as high as 30%, with high swelling ratios of 12.8−14% in pure water and 51−53% in 1 M methanol/water solution;[64−66] the high swelling ratio could seriously jeopardize membrane mechanical stability, as well as its resistance against fuel crossover.

The proton conductivity measurements of HPW−meso-silica were performed by the electrochemical impedance method over the frequency range from 1 Hz to 1 MHz in the temperature range from 20 to 90 °C under 100% RH. The HPW concentration in the meso-silica matrix varied between 0 and 83%. Figure 8a shows the proton conductivity of HPW−meso-silica nanocomposites as a function of HPW content measured at different temperatures. The meso-silica showed a very low proton conductivity of 1.4×10^{-5} S cm^{-1} at 25 °C and 3×10^{-4} S cm^{-1} at 90 °C, with a high activation energy of 46.6 kJ mol^{-1}, very close to the results reported in the literature.[41] On the other hand, the proton conductivity of mesoporous silica was enhanced significantly with HPW functionalization and increased dramatically with the HPW content in the meso-silica structure. In the case of 80% HPW−meso-silica nanocomposites, the conductivity was 0.07 S cm^{-1} at 25 °C, more than 3 orders of magnitudes higher than 1.4×10^{-5} S cm^{-1} measured on pure meso-silica. The activation energy was 14.5 kJ mol^{-1}, also much smaller than the 46.6 kJ mol^{-1} value of the pure meso-silica.

The dependence of the proton conductivity of HPW−meso-silica nanocomposites on HPW concentration measured at 25 °C is shown in Figure 8b. The proton conductivity depends strongly on the HPW content and is characterized by three regions: For nanocomposites with 0−10 wt % HPW, the proton conductivity of the HPW−meso-silica increases rapidly with the HPW content and exhibits an exponential function of HPW loading (region I). The proton conductivity was 1.4×10^{-5} S cm^{-1} for pure meso-silica and increased rapidly to 4.5×10^{-2} S cm^{-1} when 5 wt % HPW was impregnated into the meso-silica (5% HPW−meso-silica), an increase of 3 orders of magnitude in proton conductivity. When the HPW content increased to 10 wt %, the increase in the proton conductivity of the HPW−meso-silica nanocomposites became much slower (region II). With the HPW content reaching 65−67 wt %, the conductivity of HPW−meso-silica was almost independent of the HPW content and remained at a constant value of 0.07 S cm^{-1} (region III). This indicates that the threshold of HPW in the meso-silica nanocomposite is ∼10%. The maximum conductivity of the HPW−meso-silica nanocomposites based on the $Ia\bar{3}d$ structure
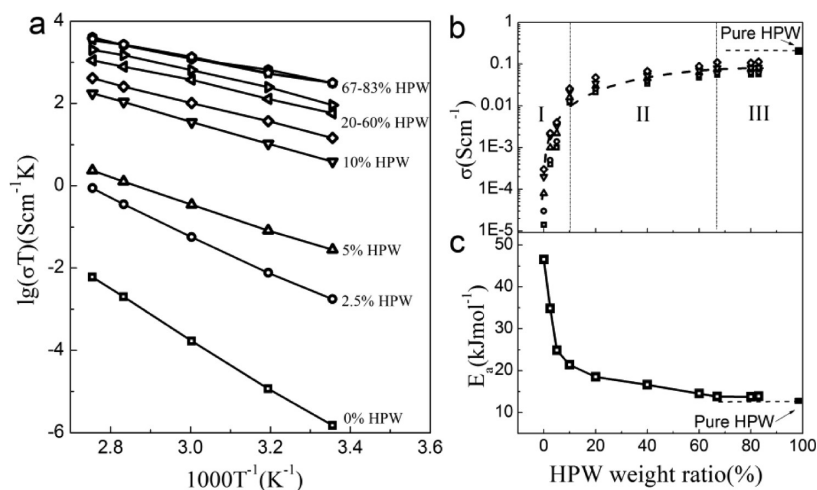
Figure 8. (a) Proton conductivity versus temperature for the HPW−meso-silica composite membranes as a function of HPW content, (b) proton conductivity versus HPW content measured at 25 °C, and (c) activation energy versus HPW content of HPW−meso-silica membrane. The conductivity and activation energy of pure HPW are from ref 67.

was ∼0.07 S cm^{-1} at 25 °C under conditions of the present study, which is lower than 0.18 S cm^{-1} for fully hydrated HPW.[67]

The activation energy (E_a) for proton conductance of HPW−meso-silica nanocomposites also depends strongly on the HPW content. As shown in Figure 8c, the dependence of the activation energy on the HPW content is also characterized by three distinct regions, similar to that observed for the conductivity. When the HPW content increased from 0% to 10%, the activation energy decreased sharply from 46.6 to 21.4 kJ mol^{-1} (region I). A further increase of the HPW content led to a more moderate decrease of E_a (region II). When the HPW content of the HPW−meso-silica nanocomposites reached 65−67 wt %, the activation energy became stable, ∼15 kJ mol^{-1}, which is also close to the ∼14.5 kJ mol^{-1} proton conductivity of fully hydrated HPW. The high proton conductivity and low activation energy indicate the establishment of an effective proton-transfer path in the HPW−meso-silica nanocomposites when the HPW content in the meso-silica reaches the threshold value of ∼10%.

The stability of the proton conductivity of a 80% HPW−meso-silica was also investigated under an accelerated durability test at 80 °C with a constant water flow rate.[51] The conductivity value of the HPW−meso-silica membranes dropped rather rapidly during the first few hours and reached a constant value being after tested for 6 h. For example, the conductivity decreased from 0.108 and stabilized at 0.075 S cm^{-1} after a 6-h test, and the loss in proton conductivity wass 28%, similar to that obtained on HPW−meso-silica nanocomposites with ∼30 wt % HPW.[51] The initial decay in the conductivity is most likely due to the leaching of HPW during the flushing of deionized water. However, the stabilized conductivity indicates the successful immobilization of water-soluble HPW in the mesoporous silica framework.

3.3. Single-Cell Performance of the HPW−Meso-Silica Nanocomposite Electrolyte Membrane. In order to demonstrate the applicability of the HPW−meso-silica membrane in fuel cells, single-cell performance tests were carried out under various operating temperatures and RH conditions in hydrogen and methanol. Figure 9 shows the single cell performance of the 80% HPW−meso-silica membrane operating in both H$_2$/O$_2$ and H$_2$/air as a function of RH at 80 °C. For the purpose of comparison, the cell performance based on Nafion 115 was also

measured in H$_2$/O$_2$ as a function of RH at 80 °C (performance curve not shown). The typical open-circuit voltage (OCV) of the cell operated in H$_2$/O$_2$ at 80 °C is 1.01 V (Figure 9a), close to that of typical single cells assembled with Nafion membranes, suggesting that the HPW−meso-silica membrane has good resistance to hydrogen crossover; The maximum power density is 308 mW cm^{-2} at 80 °C under 80% RH in H$_2$/O$_2$ and 206 mW cm^{-2} in H$_2$/air, which is quite high as compared to the values reported for inorganic membranes such as phosphoric acid doped silica, HPMo- or HPW-doped glass electrolytes, and so on.[31,68−72] The power output of the cell with HPW−meso-silica nanocomposite can be attributed to its high proton conductivity. The significant voltage drop of the cell at low currents in H$_2$/air (Figure 9b) indicates that the performance is limited by the activation polarization, particularly on the cathode side probably due to poor and not-optimized interface between the Pt/C catalyst layer and the HPW−meso-silica membrane. This suggests the cell performance can be further enhanced by the optimization of the catalyst and electrolyte interface.

Figure 9c is a comparison of the peak power density of cells with HPW−meso-silica and Nafion 115 as a function of RH, measured at 80 °C. The power density of the cells with Nafion 115 was ∼400 mW cm^{-2} under 80% RH and dropped significantly to ∼38 mW cm^{-2} when the RH was decreased to 20%, a reduction in power output by 90%. The substantial reduction in power output of Nafion 115 with the decrease in RH is clearly due to the fact that the proton conductivity of Nafion membranes decreases significantly with decreasing RH.[8,12,73] In contrast to the Nafion 115 membrane, cells with HPW−meso-silica nanocomposite membranes showed a much smaller variation as a function of RH. Under 80% RH, the power density of HPW−meso-silica membrane was 308 mW cm^{-2} in H$_2$/O$_2$, and it was 215 mW cm^{-2} as the RH decreased to 20%. The decrease in power output was 30%, which is 3 times smaller as compared to that of the cell with Nafion 115 membranes. A similar dependence of the power output on the RH was also observed for the HPW−meso-silica cells operated in H$_2$/air. The highly stable performance of HPW−meso-silica nanocomposites indicates that the proton conductivity of the HPW−meso-silica nanocomposites does not change significantly with the change in
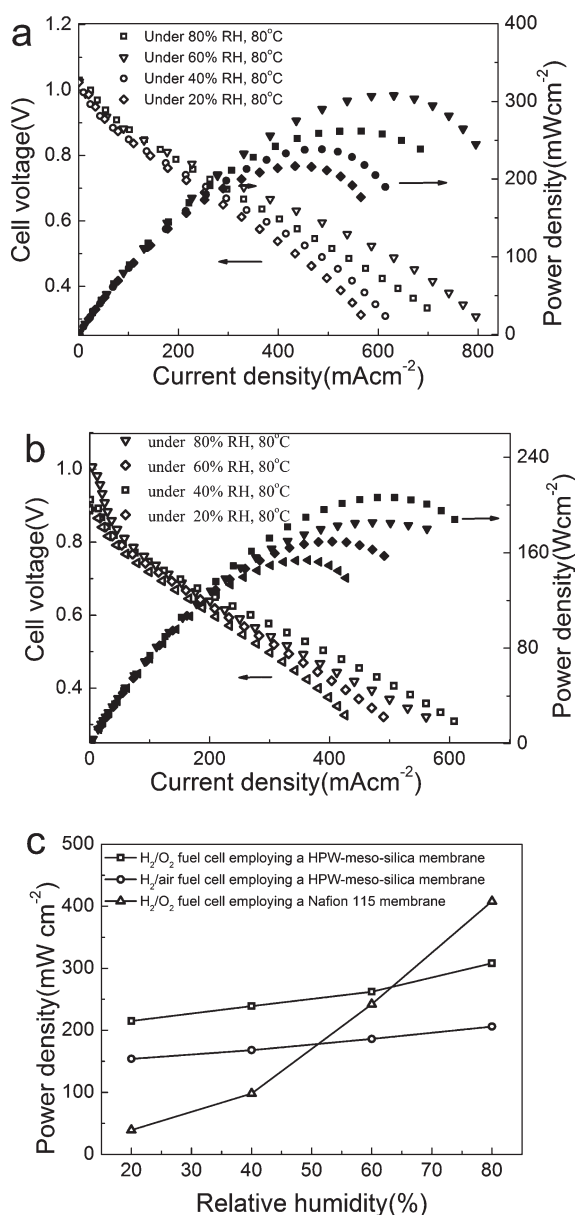
Figure 9. Polarization and power density of single cells employing an 80% HPW−meso-silica nanocomposite membrane in (a) H_2/O_2 and (b) H_2/air at 80 °C under different RH values. (c) Plot of the dependence on RH of the maximum power density of cells with 80% HPW−meso-silica and Nafion 115 membranes. The Pt catalyst loading was 0.4 mg cm^{-2} for both the anode and cathode.

Figure 10. (a) Methanol crossover limiting current curves of an 80% HPW−meso-silica nanocomposite membrane measured at different temperatures, (b) polarization and power density of single cells employing a 67% HPW−meso-silica membrane in methanol/air at different temperatures without external humidification, and (c) cell stability measured at a constant cell potential of 0.50 V at 150 °C in methanol/air without external humidification.

RH, clearly demonstrating the high water retention capability of the HPW−meso-silica nanocomposites. The lower performance of HPW−meso-silica nanocomposites as compared to Nafion 115 in the high-RH region might also be due to the fact HPW−meso-silica nanocomposite membranes were significantly thicker than the Nafion 115 used in this study (500 μm verse 125 μm).

Figure 10a shows the methanol crossover current curves in an 80% HPW−meso-silica membrane. The limiting current of methanol oxidation with the HPW−meso-silica membranes was 16 mA cm^{-2} at 80 °C and increased to 27 mA cm^{-2} at 160 °C. The methanol crossover limiting currents were significantly lower than those of Nafion membranes. For example, the limiting crossover current
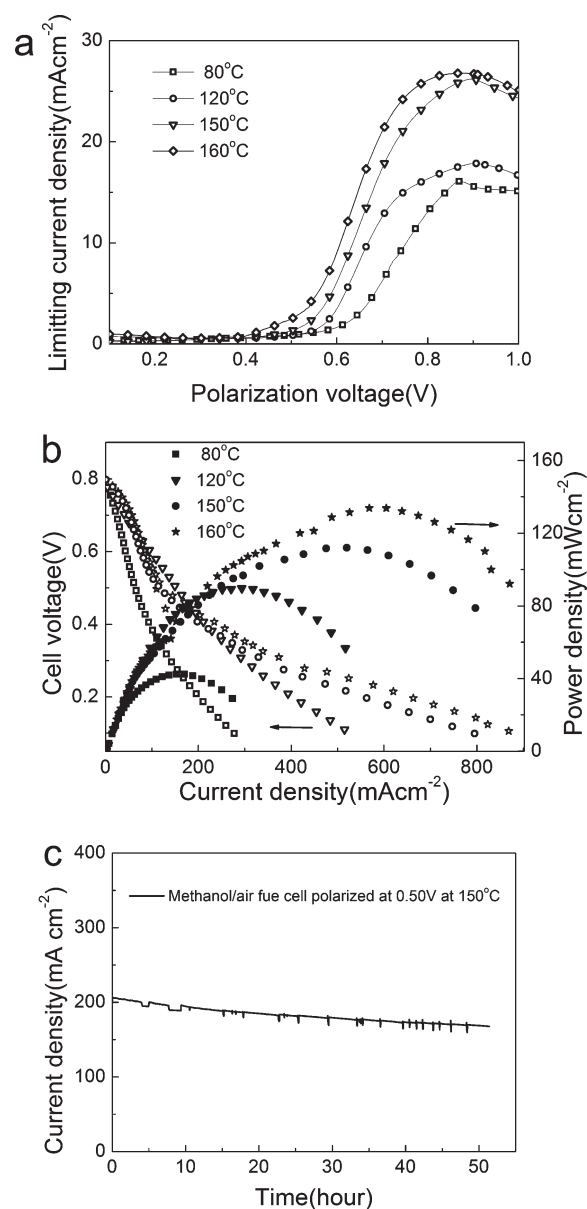
was 98 mA cm^{-2} on a Nafion 1135 membrane (89 μm in thickness) measured at room temperature[74] and 277 mA cm^{-2} on a Nafion 117 membrane (178 μm in thickness) measured at 80 °C in a 2 M methanol solution.[75] The much lower methanol crossover current on the HPW−meso-silica membrane could also be related to the gas-phase diffusion of methanol and the much thicker HPW−meso-silica membranes ($\sim$500 μm in this case). Another important reason is the fact that the size of the mesopores or channels of HPW−meso-silica nanocomposites was in the range of 3.7−4.9 nm and did not swell with the water content or humidity like in the case of Nafion membranes.[64−66,76]

The performance of cells with a 67% HPW—meso-silica nanocomposite membrane was measured in methanol fuel with no external humidifier on the air side (Figure 10b). The OCV of the cell in methanol/air was ~0.80 V, lower than 0.9—1.0 V observed for H_2/air. The low OCV for the cell in methanol as compared with that in hydrogen might be due to the methanol crossover (see Figure 10a). The maximum power output was 43 mW cm^{-2} at 80 °C and increased to 134 mW cm^{-2} as the temperature increased to 160 °C. This shows that the increase in the operating temperature is beneficial for DMFCs. In the case of methanol fuel, the CH_3OH solution (2 M) is gasified after entering the anode chamber, and the water-to methanol molar ratio is 9 to 1. The high water/methanol ratio could help to maintain a certain hydration level on the anode side of the cell. The decrease in the cell polarization potential in the low-current region is substantial in methanol/air as compared to that in H_2/air (Figure 9b), indicating the significant activation polarization losses for the methanol oxidation reaction. The performance of DMFCs based on HPW—meso-silica nanocomposite membranes is most likely limited by the methanol oxidation reaction in addition to the oxygen reduction reaction probably because of the unoptimized electrocatalysts for both anode and cathode at high temperatures. However, the cell with the HPW—meso-silica nanocomposite membranes showed a reasonable stability, as shown in Figure 10b, measured under a constant potential of 0.5 V at 150 °C for 51.5 h. The fuel cell experienced a gradual drop in current density, with a degradation rate of 0.6 mA h^{-1} over the test period. Nevertheless, the stability of the cell is reasonable considering that the catalyst and HPW—meso-silica membrane interface are far from optimized. The high power density over the range of RH values studied and the good stability indicate the applicability of the HPW—meso-silica nanocomposite as high-temperature PEM for fuel cells.

3.4. Proton Transfer in HPW—Meso-Silica Nanocomposites. The low activation energy and high proton conductivity of HPW—meso-silica nanocomposites in the present study indicate that water plays an important role in the proton-transfer process because the presence of water significantly reduces the activation barrier to proton movement. The increase of proton mobility enhanced by small amounts of water has been explained by quantum chemical DFT calculations.[77] Without water molecule consideration, the barrier to the motion of protons on an isolated HPW is significantly high, owing to the larger distance over which transfer must occur between two bridging oxygen atoms. The zero-point-vibrational-energy- (ZPVE-) corrected activation energy for anhydrous proton movement through the individual HPW clusters was calculated to be 103.3 kJ mol^{-1}.[77] After water adsorption, a second hydrogen bond would be formed between the hydrogen atom of the water molecule and a terminal oxygen atom site of the Keggin unit (KU) in addition to the hydrogen bonding between the proton of the KU and the oxygen atom of the water molecule. Herein, the barrier was greatly reduced by an order of magnitude to ~14.5 kJ mol^{-1} under 100% RH, as shown in the present study. The significantly low activation energy, together with the high conductivity is most likely due to the water-promoted proton hopping pathway, which does not require substantial structural rearrangement of the Keggin unit to form the transition state. The much smaller reduction in the performance of HPW—meso-silica nanocomposites with the RH change, in comparison with that of Nafion membranes, clearly demonstrates the high water retention capability of the HPW—meso-silica nanocomposites. The high water

retention properties of HPW—meso-silica nanocomposites are also supported by the observed good stability of the cell in methanol/air without external humidification. The high water retention properties of HPW—meso-silica can be attributed to the ordered mesoporous silica structure and the possible interaction between the Keggin anions and meso-silica, leading to the formation of $(\equiv SiOH_2^+)(H_2PW_{12}O_{40}^-)$ species.[59] However, the present study would not be sufficient to conclude whether the proton transfer in the HPW—meso-silica nanocomposites occurs by Grotthuss or vehicle mechanisms or a combination of the two. More work is needed to fundamentally understanding the proton-transfer mechanism in HPW—meso-silica nanocomposite systems.

4. CONCLUSIONS

A novel inorganic proton-exchange membrane based on the HPW—meso-silica nanocomposite was characterized in detail. The results indicate the formation of an ordered three-dimensional mesoporous framework with HPW molecules anchored in the mesoporous silica matrix, forming an effective proton conduction pathway. The HPW—meso-silica electrolyte shows a high proton conductivity of 0.07 S cm^{-1} at 25 °C with a low activation energy of 14.5 kJ mol^{-1}. A single cell based on a HPW—meso-silica membrane produced a peak power of 134 mW cm^{-2} in methanol/air at 160 °C without humidification, as well as a peak power of 308 mW cm^{-2} in H_2/O_2 and 206 mW cm^{-2} in H_2/air at 80 °C and 80% RH. The high tolerance of HPW—meso-silica nanocomposites toward RH changes, in comparison with that of Nafion membranes, clearly demonstrates the high water retention capability of HPW—meso-silica nanocomposites. The present study demonstrates that inorganic proton-exchange membranes with high proton conductivities can be realized with HPW—meso-silica nanocomposites and can be used as effective proton-exchange membranes for high-temperature PEMFCs and DMFCs.

■ AUTHOR INFORMATION

Corresponding Author
*E-mail: s.jiang@curtin.edu.au.

■ REFERENCES

(1) Bauen, A.; Hart, D. *J. Power Sources* **2000**, *86*, 482.

(2) Steele, B. C. H.; Heinzel, A. *Nature* **2001**, *414*, 345.

(3) Yang, C.; Costamagna, P.; Srinivasan, S.; Benziger, J.; Bocarsly, A. B. *J. Power Sources* **2001**, *103*, 1.

(4) Li, Q. F.; He, R. H.; Jensen, J. O.; Bjerrum, N. J. *Chem. Mater.* **2003**, *15*, 4896.

(5) Zhang, J. L.; Xie, Z.; Zhang, J. J.; Tanga, Y. H.; Song, C. J.; Navessin, T.; Shi, Z. Q.; Song, D. T.; Wang, H. J.; Wilkinson, D. P.; Liu, Z. S.; Holdcroft, S. *J. Power Sources* **2006**, *160*, 872.

(6) Ahmad, H.; Kamarudin, S. K.; Hasran, U. A.; Daud, W. R. W. *Int. J. Hydrogen Energy* **2010**, *35*, 2160.

(7) Neburchilov, V.; Martin, J.; Wang, H. J.; Zhang, J. J. *J. Power Sources* **2007**, *169*, 221.

(8) Zawodzinski, T. A.; Springer, T. E.; Davey, J.; Jestel, R.; Lopez, C.; Valerio, J.; Gottesfeld, S. *J. Electrochem. Soc.* **1993**, *140*, 1981.

11862

dx.doi.org/10.1021/jp201250r |*J. Phys. Chem. C* 2011, 115, 11854–11863

(9) Yang, C.; Srinivasan, S.; Bocarsly, A. B.; Tulyani, S.; Benziger, J. B. *J. Membr. Sci.* **2004**, *237*, 145.

(10) Sone, Y.; Ekdunge, P.; Simonsson, D. *J. Electrochem. Soc.* **1996**, *143*, 1254.

(11) Hickner, M. A.; Ghassemi, H.; Kim, Y. S.; Einsla, B. R.; McGrath, J. E. *Chem. Rev.* **2004**, *104*, 4587.

(12) Yan, X. M.; Mei, P.; Mi, Y. Z.; Gao, L.; Qin, S. X. *Electrochem. Commun.* **2009**, *11*, 71.

(13) Ciureanu, M. *J. Appl. Electrochem.* **2004**, *34*, 705.

(14) Kozhevnikov, I. V. *Chem. Rev.* **1998**, *98*, 171.

(15) Misono, M. *Catal. Rev.-Sci. Eng.* **1987**, *29*, 269.

(16) Cui, Z. M.; Xing, W.; Liu, C. P.; Tian, D.; Zhang, H. *J. Power Sources* **2010**, *195*, 1619.

(17) Kulesza, P. J.; Chojak, M.; Karnicka, K.; Miecznikowski, K.; Palys, B.; Lewera, A.; Wieckowski, A. *Chem. Mater.* **2004**, *16*, 4128.

(18) Barczuk, P. J.; Tsuchiya, H.; Macak, J. M.; Schmuki, P.; Szymanska, D.; Makowski, O.; Miecznikowski, K.; Kulesza, P. J. *Electrochem. Solid State Lett.* **2006**, *9*, E13.

(19) Ferrell, J. R.; Kuo, M. C.; Turner, J. A.; Herring, A. M. *Electrochim. Acta* **2008**, *53*, 4927.

(20) Barczuk, P. J.; Lewera, A.; Miecznikowski, K.; Zurowski, A.; Kulesza, P. J. *J. Power Sources* **2010**, *195*, 2507.

(21) Barczuk, P. J.; Lewera, A.; Skorupska, K.; Jiang, S. P.; Li, C. M.; Kulesza, P. J. *Electrocatalysis* **2011**, *2*, 52.

(22) Wlodarczyk, R.; Chojak, M.; Miecnikowski, K.; Kolary, A.; Kulesza, P. J.; Marassi, R. *J. Power Sources* **2006**, *159*, 802.

(23) Wlodarczyk, R.; Kolary-Zurowska, A.; Marassi, R.; Chojak, M.; Kulesza, P. J. *Electrochim. Acta* **2007**, *52*, 3958.

(24) Wang, D. L.; Lu, S. F.; Jiang, S. P. *Chem. Commun.* **2010**, *46*, 2058.

(25) Stanis, R. J.; Kuo, M. C.; Rickett, A. J.; Turner, J. A.; Herring, A. M. *Electrochim. Acta* **2008**, *53*, 8277.

(26) Tatsumisago, M.; Honjo, H.; Sakai, Y.; Minami, T. *Solid State Ionics* **1994**, *74*, 105.

(27) Rao, P. M.; Wolfson, A.; Kababya, S.; Vega, S.; Landau, M. V. *J. Catal.* **2005**, *232*, 210.

(28) Rao, P. M.; Wolfson, A.; Landau, M. V.; Herskowitz, M. *Catal. Commun.* **2004**, *5*, 327.

(29) Mikhailenko, S. D.; Kaliaguine, S.; Moffat, J. B. *Solid State Ionics* **1997**, *99*, 281.

(30) Uma, T.; Nogami, M. *Chem. Mater.* **2007**, *19*, 3604.

(31) Uma, T.; Nogami, M. *Anal. Chem.* **2008**, *80*, 506.

(32) Li, Z. Y.; Zhang, Q.; Liu, H. T.; He, P.; Xu, X. D.; Li, J. H. *J. Power Sources* **2006**, *158*, 103.

(33) Yamada, M.; Honma, I. *J. Phys. Chem. B* **2006**, *110*, 20486.

(34) Staiti, P.; Arico, A. S.; Baglio, V.; Lufrano, F.; Passalacqua, E.; Antonucci, V. *Solid State Ionics* **2001**, *145*, 101.

(35) Celso, F.; Mikhailenko, S. D.; Kaliaguine, S.; Duarte, U. L.; Mauler, R. S.; Gomes, A. S. *J. Membr. Sci.* **2009**, *336*, 118.

(36) Cui, Z. M.; Xing, W.; Liu, C. P.; Liao, J. H.; Zhang, H. *J. Power Sources* **2009**, *188*, 24.

(37) Oh, S. Y.; Yoshida, T.; Kawamura, G.; Muto, H.; Sakai, M.; Matsuda, A. *J. Mater. Chem.* **2010**, *20*, 6359.

(38) Lakshminarayana, G.; Nogami, M. *J. Phys. Chem. C* **2009**, *113*, 14540.

(39) Sweikart, M. A.; Herring, A. M.; Turner, J. A.; Williamson, D. L.; McCloskey, B. D.; Boonrueng, S. R.; Sanchez, M. *J. Electrochem. Soc.* **2005**, *152*, A98.

(40) Tan, A. R.; de Carvalho, L. M.; Gomes, A. D. *Macromol. Symp.* **2005**, *229*, 168.

(41) Li, H. B.; Nogami, M. *Adv. Mater.* **2002**, *14*, 912.

(42) Athens, G. L.; Ein-Eli, Y.; Chmelka, B. F. *Adv. Mater.* **2007**, *19*, 2580.

(43) Colomer, M. T. *Adv. Mater.* **2006**, *18*, 371.

(44) Yamada, M.; Li, D. L.; Honma, I.; Zhou, H. S. *J. Am. Chem. Soc.* **2005**, *127*, 13092.

(45) Daiko, Y.; Kasuga, T.; Nogami, M. *Chem. Mater.* **2002**, *14*, 4624.

(46) Li, H. B.; Nogami, M. *Chem. Commun.* **2003**, 236.

(47) Xiong, L. M.; Nogami, M. *Chem. Lett.* **2006**, *35*, 972.

(48) Vichi, F. M.; Tejedor-Tejedor, M. I.; Anderson, M. A. *Chem. Mater.* **2000**, *12*, 1762.

(49) Halla, J. D.; Mamak, M.; Williams, D. E.; Ozin, G. A. *Adv. Funct. Mater.* **2003**, *13*, 133.

(50) Bocquet, L.; Charlaix, E.; Ciliberto, S.; Crassous, J. *Nature* **1998**, *396*, 735.

(51) Lu, S. F.; Wang, D. L.; Jiang, S. P.; Xiang, Y.; Lu, J. L.; Zeng, J. *Adv. Mater.* **2010**, *22*, 971.

(52) Tang, H. L.; Pan, M.; Lu, S. F.; Lu, J. L.; Jiang, S. P. *Chem. Commun.* **2010**, *46*, 4351.

(53) Li, Z.; Chen, D. H.; Tu, B.; Zhao, D. Y. *Microporous Mesoporous Mater.* **2007**, *105*, 34.

(54) Chen, D.; Li, Z.; Yu, C.; Shi, Y.; Zhang, Z.; Tu, B.; Zhao, D. *Chem. Mater.* **2005**, *17*, 3228.

(55) Kim, T. W.; Kleitz, F.; Paul, B.; Ryoo, R. *J. Am. Chem. Soc.* **2005**, *127*, 7601.

(56) Yang, J.; Janik, M. J.; Ma, D.; Zheng, A. M.; Zhang, M. J.; Neurock, M.; Davis, R. J.; Ye, C. H.; Deng, F. *J. Am. Chem. Soc.* **2005**, *127*, 18274.

(57) Kim, Y. S.; Wang, F.; Hickner, M.; Zawodzinski, T. A.; McGrath, J. E. *J. Membr. Sci.* **2003**, *212*, 263.

(58) Rocchiccioli-Deltcheff, C.; Fournier, M.; Franck, R.; Thouvenot, R. *Inorg. Chem.* **1983**, *22*, 207.

(59) Dias, A. S.; Pillinger, M.; Valente, A. A. *Microporous Mesoporous Mater.* **2006**, *94*, 214.

(60) Lefebvre, F. *J. Chem. Soc., Chem. Commun.* **1992**, 756.

(61) Gregg, S. J.; Sing, K. S. W. *Adsorption, Surface Area and Porosity*, 2nd ed.; Academic Press: London, 1991.

(62) Xu, Y. W.; Wu, Z. X.; Zhang, L. J.; Lu, H. J.; Yang, P. Y.; Webley, P. A.; Zhao, D. Y. *Anal. Chem.* **2009**, *81*, 503.

(63) Rao, P. M.; Goldberg-Oppenheimer, P.; Kababya, S.; Vega, S.; Landau, M. J. *Mol. Catal. A: Chem.* **2007**, *275*, 214.

(64) Tazi, B.; Savadogo, O. *Electrochim. Acta* **2000**, *45*, 4329.

(65) Randov, A.; Hovorka, S.; Izak, P.; Bartovsk, L. *J. Electroanal. Chem.* **2008**, *616*, 117.

(66) Gebel, G.; Aldebert, P.; Pineri, M. *Polymer* **1993**, *34*, 333.

(67) Nakamura, O.; Kodama, T.; Ogino, I. *Chem. Lett.* **1979**, 17.

(68) Nakanishi, T.; Norisuye, T.; Sato, H.; Takemori, T.; Tran-Cong-Miyata, Q.; Sugimoto, T.; Nomura, S. *Macromolecules* **2007**, *40*, 4165.

(69) Xiong, L.; Yang, Y.; Shi, J.; Nogami, M. *Microporous Mesoporous Mater.* **2008**, *111*, 343.

(70) Uma, T.; Nogami, M. *J. Membr. Sci.* **2008**, *323*, 11.

(71) Inoue, T.; Uma, T.; Nogami, M. *J. Membr. Sci.* **2008**, *323*, 148.

(72) Uma, T.; Nogami, M. *Fuel Cells* **2007**, *7*, 279.

(73) Buchi, F. N.; Scherer, G. G. *J. Electrochem. Soc.* **2001**, *148*, A183.

(74) Jiang, S. P.; Liu, Z. C.; Tian, Z. Q. *Adv. Mater.* **2006**, *18*, 1068.

(75) Ren, X.; Springer, T. E.; Gottesfeld, S. *J. Electrochem. Soc.* **2000**, *147*, 92.

(76) Divisek, J.; Eikerling, M.; Mazin, V.; Schmitz, H.; Stimming, U.; Volfkovich, Y. M. *J. Electrochem. Soc.* **1998**, *145*, 2677.

(77) Janik, M. J.; Davis, R. J.; Neurock, M. *J. Am. Chem. Soc.* **2005**, *127*, 5238.